Supplementary Information for:

Simple and Low-Cost Ionic Plastic Crystal for Multipurpose Cold-Storage and Barocaloric Thermal Management

*Pedro Dafonte-Rodríguez, [a] Ángel Ferradanes-Martínez, [a] Julian Walker, [b] Javier García-Ben, [a] Charles James McMonagle, [c] Socorro Castro-García,[a] María Antonia Señarís-Rodríguez,[a] Manuel Sánchez-Andújar *[a] and Juan Manuel Bermúdez-García *[a]*

[a] CICA – Centro Interdisciplinar de Química e Bioloxía and Departamento de Química, Facultade de Ciencias, Universidade da Coruña, Campus de Elviña, 15071, A Coruña, Spain.

[b] Norwegian University of Science and Technology, Department of Materials Science and Engineering, Trondheim 7491, Norway.

[c] European Synchrotron Radiation Facility, Swiss-Norwegian Beamlines, Grenoble 3843, France.

E-mail: m.andujar@udc.es; j.bermudez@udc.es

Contents

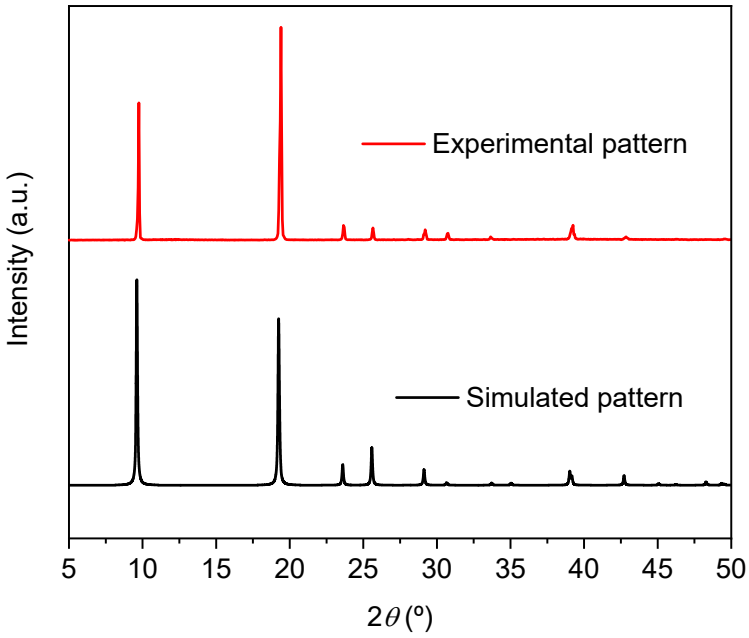

Figure S1. Room temperature experimental PXRD patterns for the obtained $[CH_3NH_3][BF_4]$ compound compared with the simulated pattern based on the reported single crystal structure at room temperature.

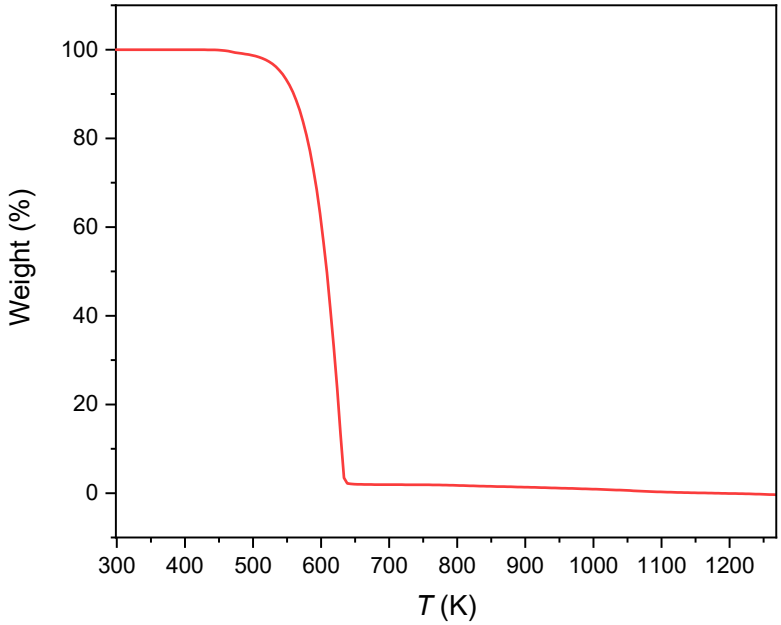

Figure S2. Thermogravimetric analysis of $[CH_3NH_3][BF_4]$ under N_2 atmosphere.

(a)

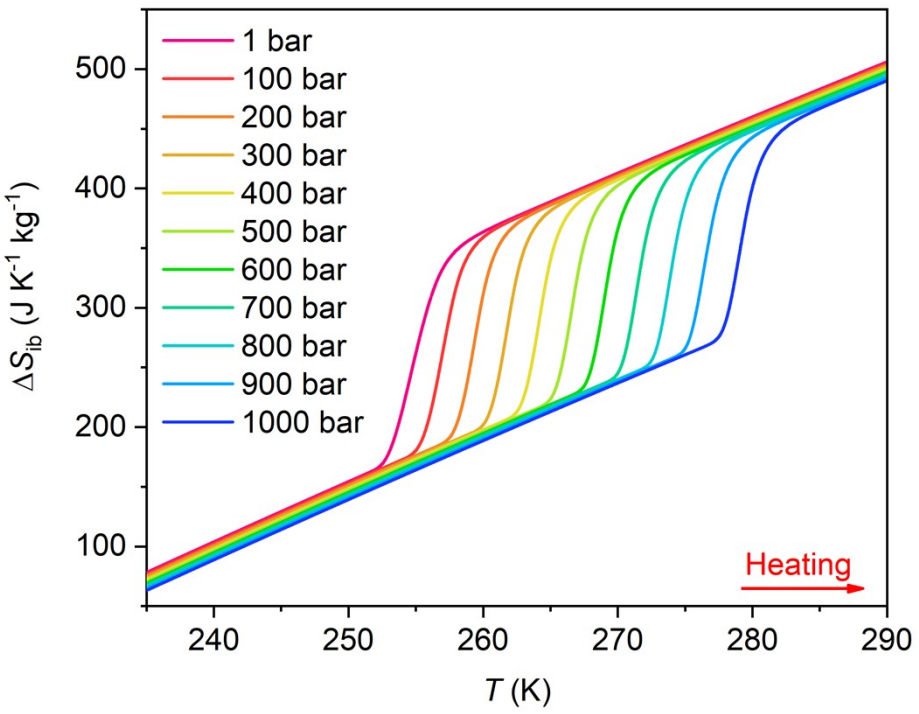

(b)

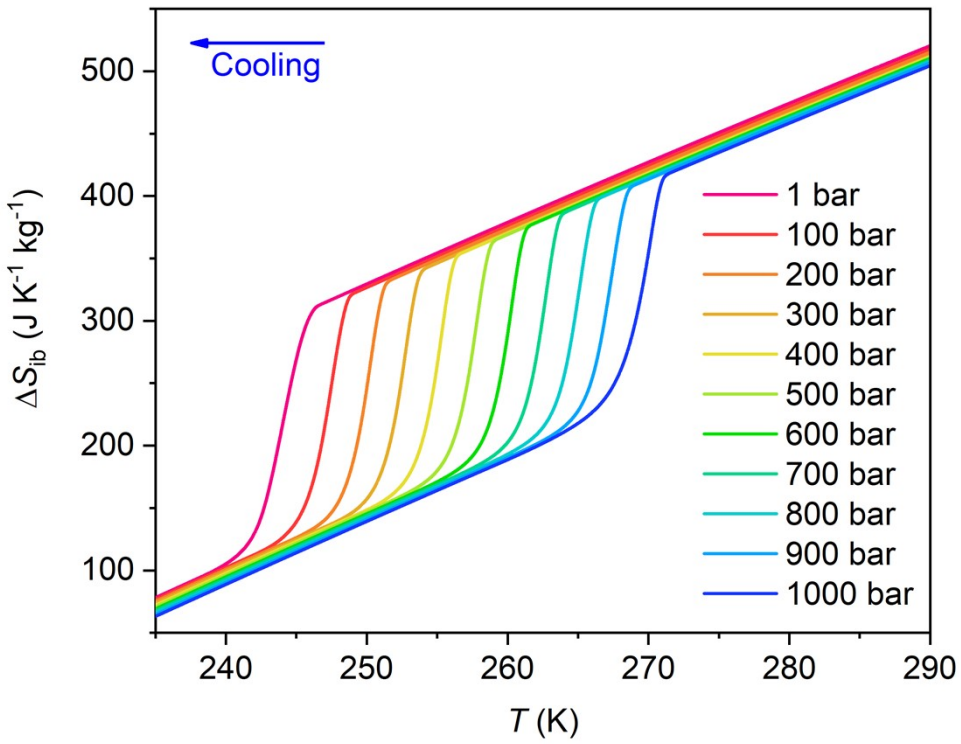

Figure S3. ΔS_{ib} at different isobaric conditions during (a) heating and (b) cooling.

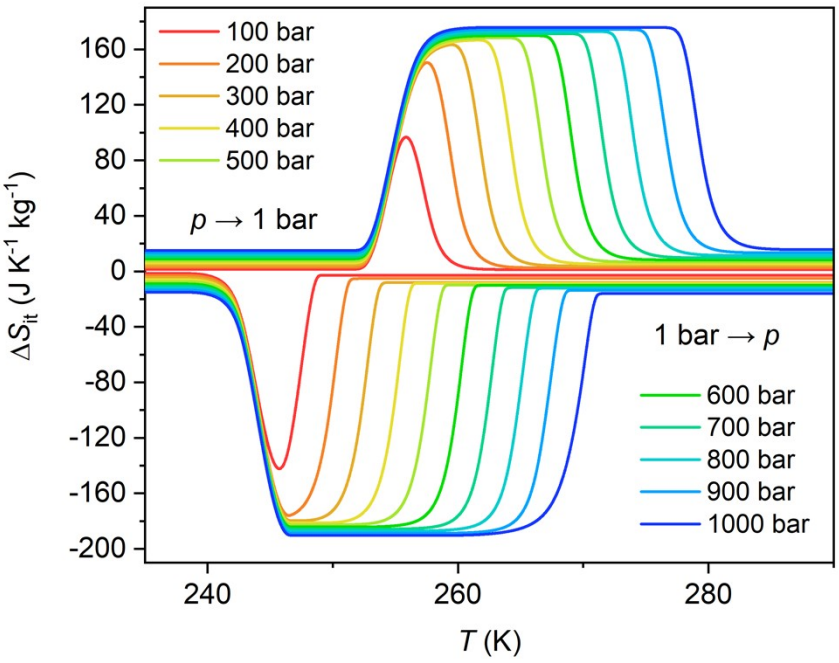

Figure S4. Irreversible pressure-driven isothermal entropy changes (ΔS_{it}) on compression (1 bar→p) and decompression (p→1 bar).

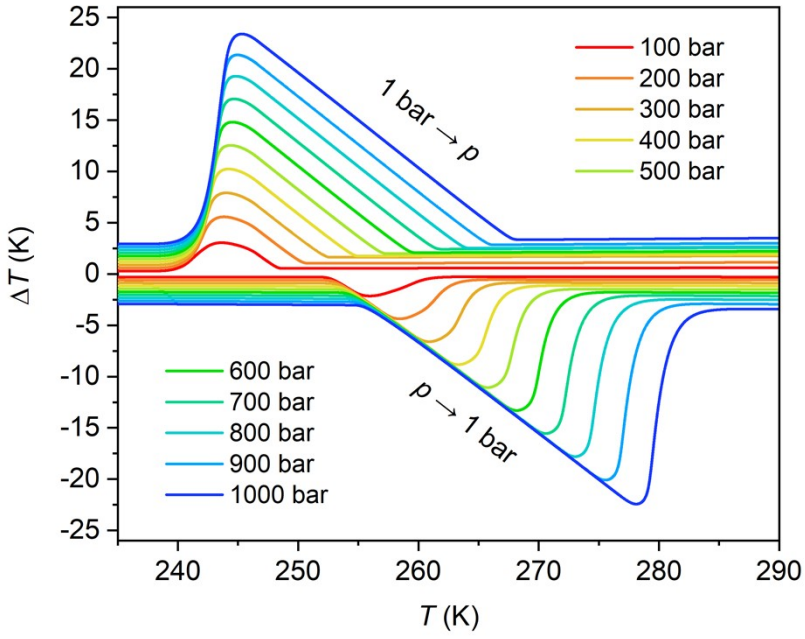

Figure S5. Irreversible adiabatic temperature (ΔT) changes on applying (1 bar → p) and removing (p → 1 bar) pressure at different isobaric pressures.

(a)

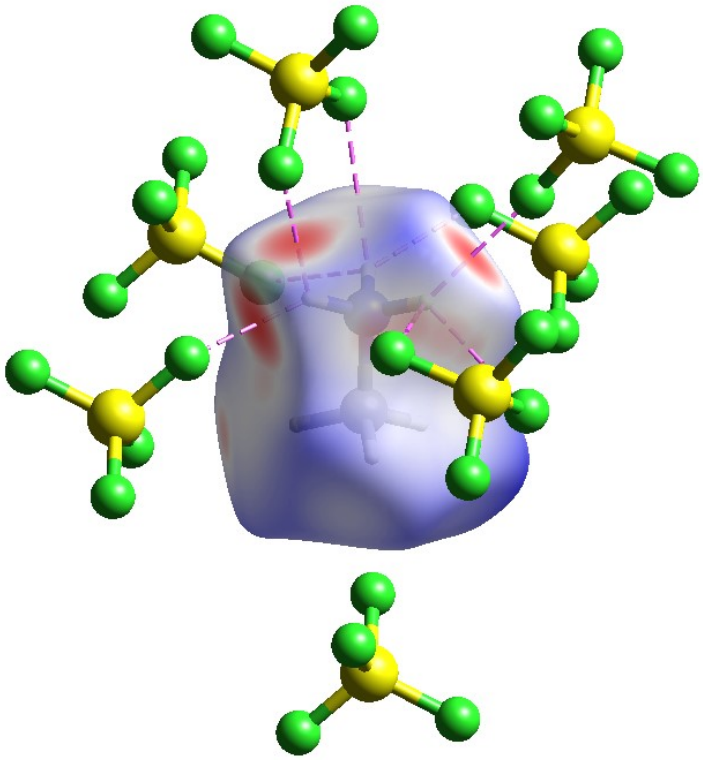

(b)

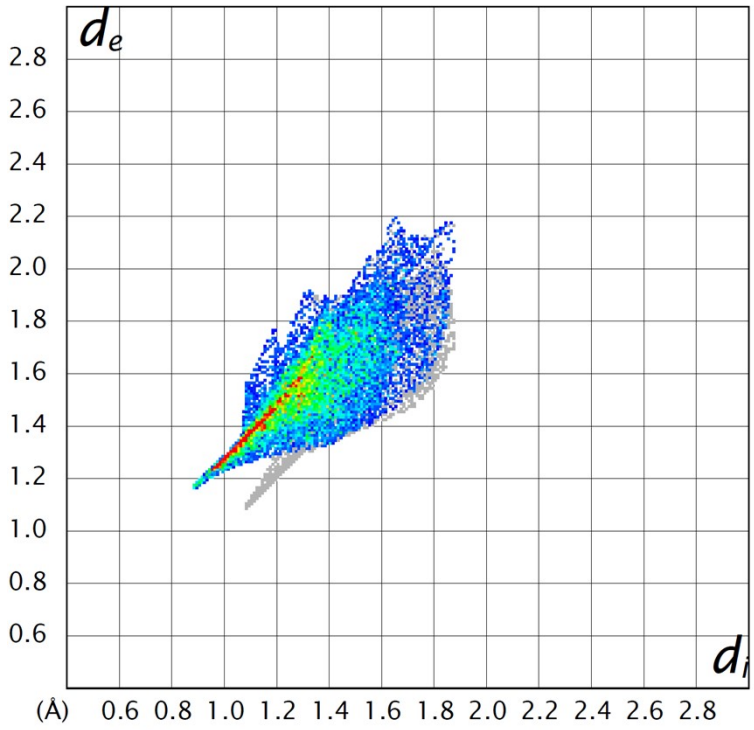

Figure S6. (a) Hirshfield surface analysis of $[CH_3NH_3]^+$ cations, showing the d_{norm} surface and (b) two-dimensional fingerprint plot showing the F···H interactions.

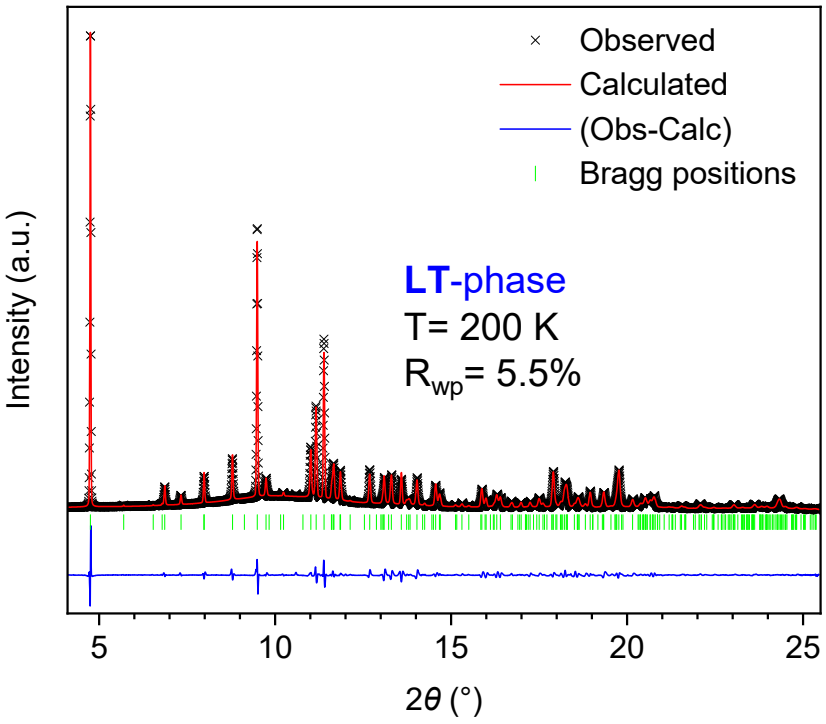

Figure S7. Le Bail refinement of LT-phase of $[CH_3NH_3][BF_4]$ at T = 200 K.

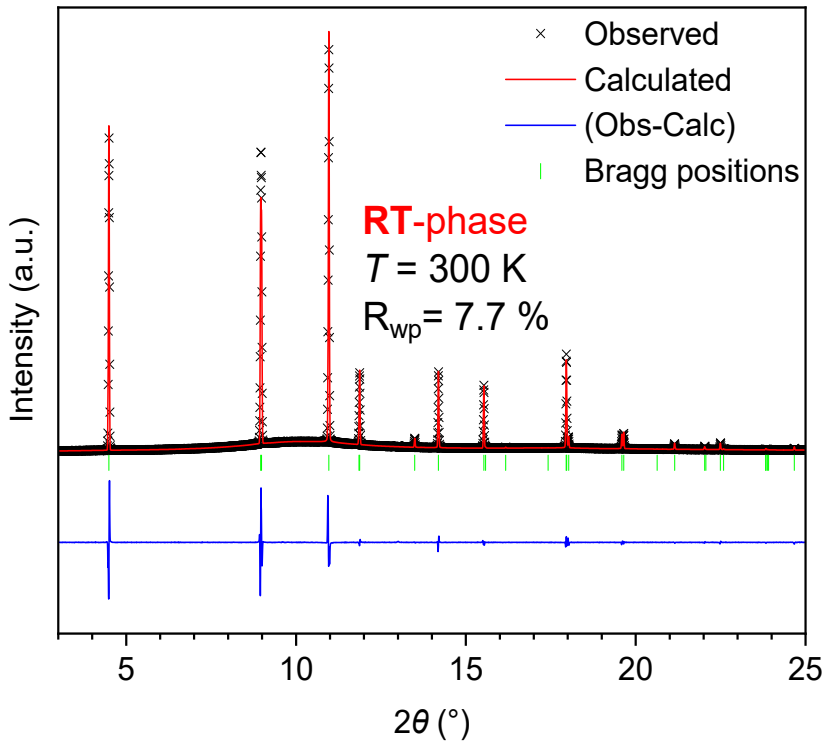

Figure S8. Le Bail refinement of RT-phase of $[CH_3NH_3][BF_4]$ at T = 300 K.

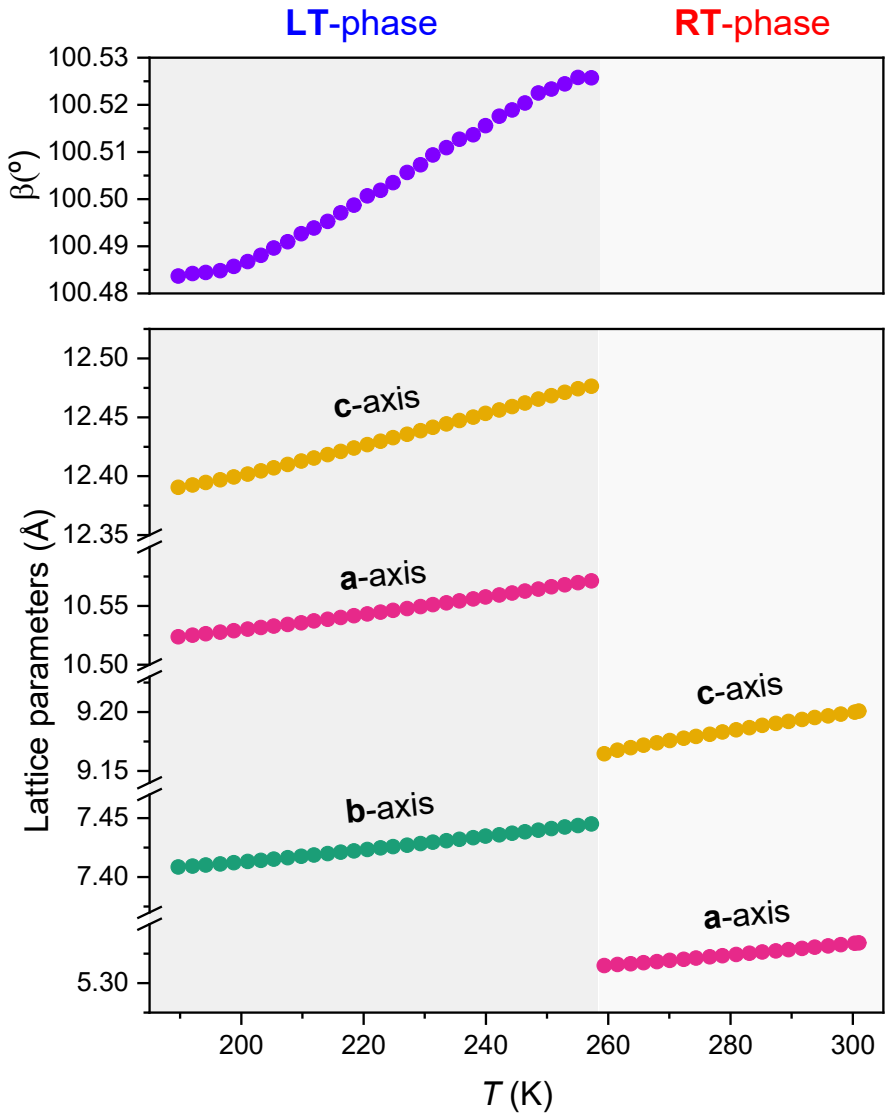

Figure S9. Evolution of the lattice parameters of $[CH_3NH_3][BF_4]$ as a function of temperature.

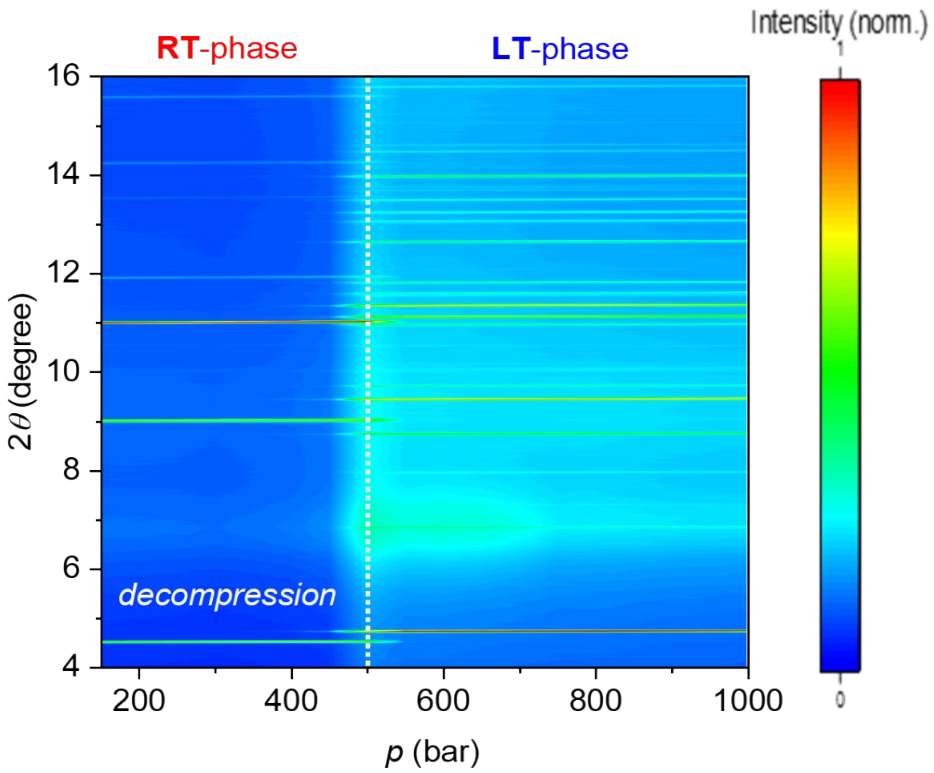

Figure S10. Contour plot of SPXRD patterns under decompression at T = 264 K.

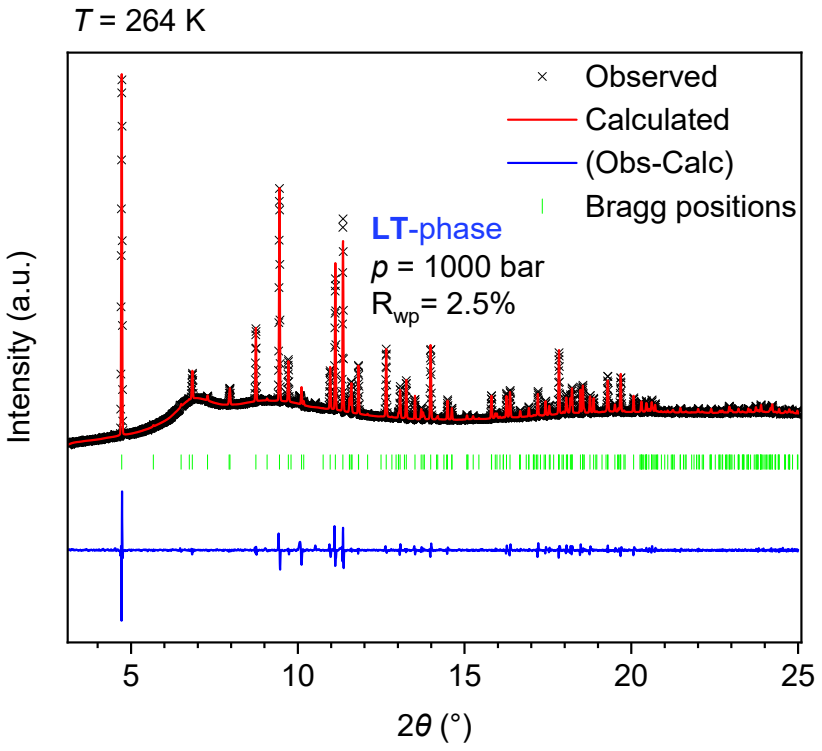

Figure S11. Le Bail refinement of LT-phase of $[CH_3NH_3][BF_4]$ at p = 1000 bar and T = 264 K .

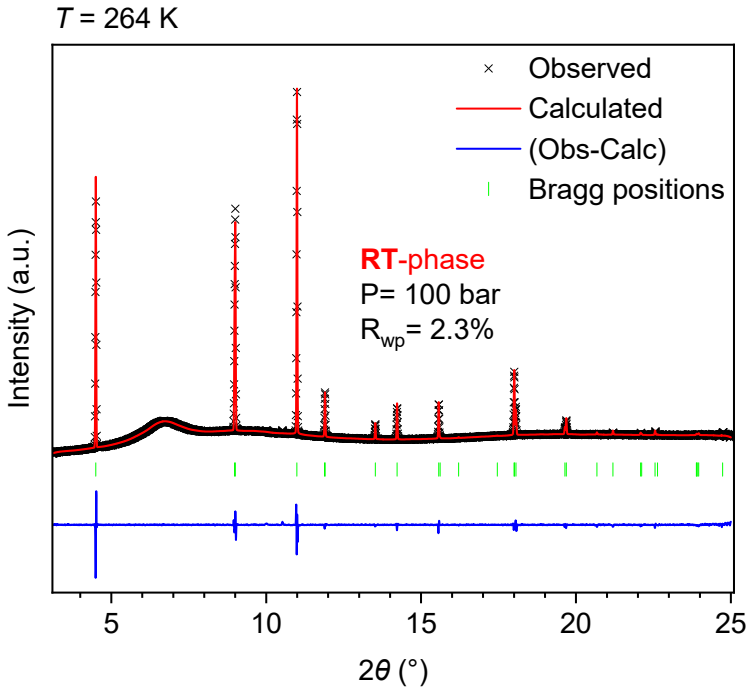

Figure S12. Le Bail refinement of RT-phase of $[CH_3NH_3][BF_4]$ at p = 1000 bar and T = 264 K .

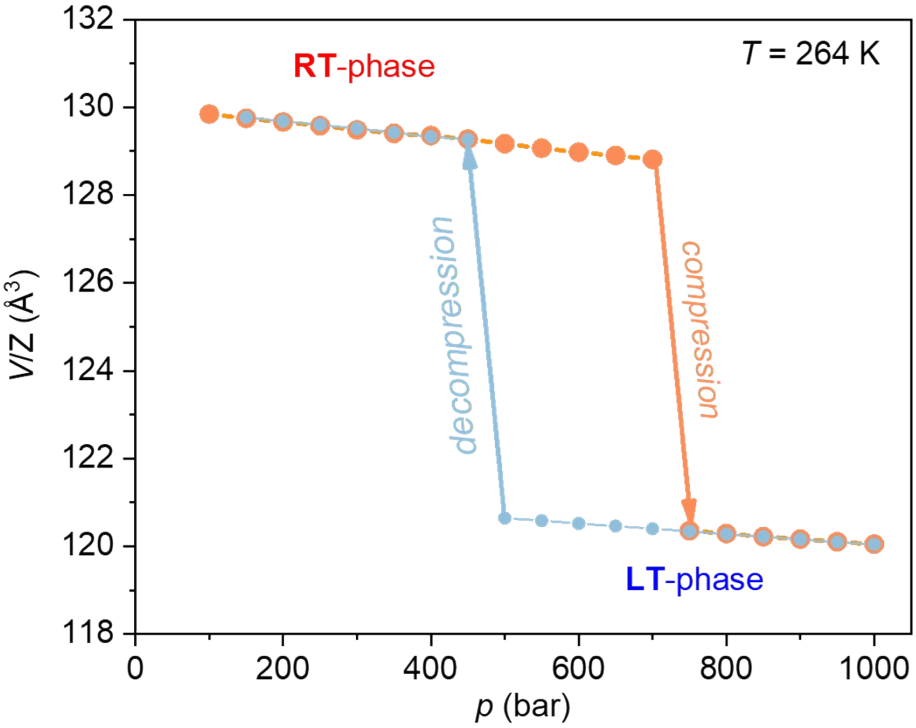

Figure S13. Cell volume of the $[CH_3NH_3][BF_4]$ compound under compression and decompression at T = 264 K.

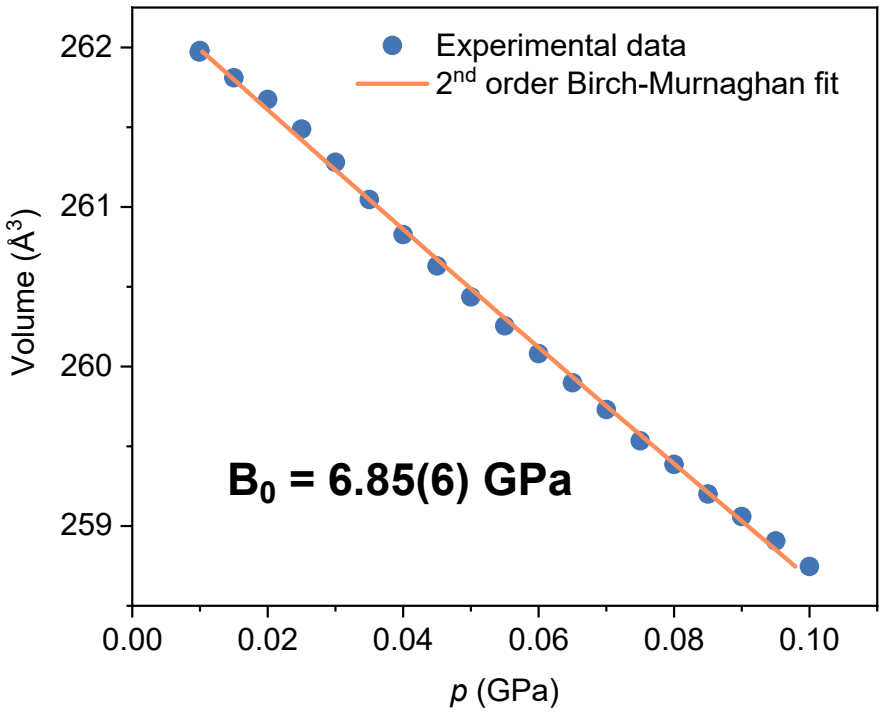

Figure S14. Experimental volume vs. pressure data for the RT-phase collected at room temperature (blue dots) and fit of the second-order Birch-Murnaghan equation of state for the estimation of the isothermal bulk modulus.

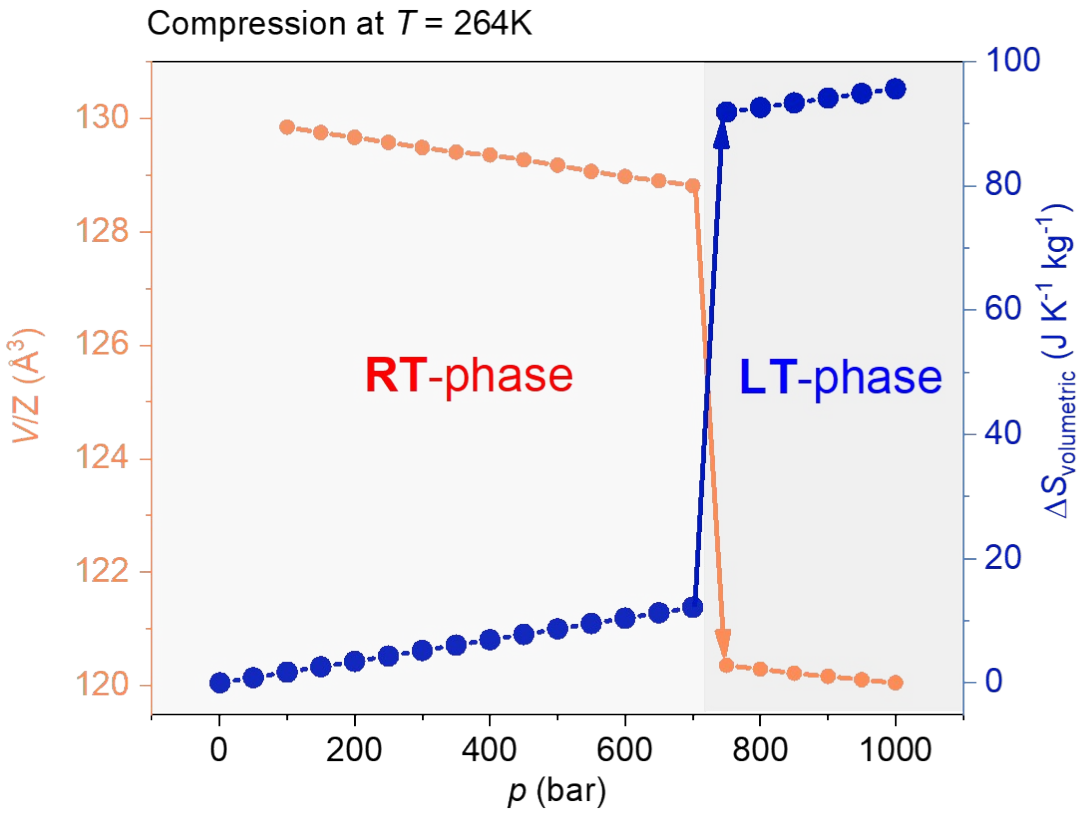

Figure S15. Evolution of the volume of LT- and RT-phase of $[CH_3NH_3][BF_4]$ compound as a function of pressure in compression and volumetric entropy change associated with the volume change at the phase transition and the elastic entropy change due the lattice shrinkage on either side of the phase transition at T = 264 K.

Table S1. Price comparison in euros per gram (€/g) for different commercial plastic crystals reported for barocaloric and/or thermal energy storage applications, in comparison with [DBA][BF4] and the $[CH_3NH_3][BF_4]$ compound. [1–8] Prices were consulted in March 2026.

Material	CAS number	Price per gram	Consulted Supplier	Reference
C_{60}	99685-96-8	346.00 €/g	Fisher Scientific	[1]
m-carborane	16986-24-6	195.00€/g	abcr GmbH	[2]
o-carborane	16872-09-6	116.00 €/g	abcr GmbH	[2]
$[N_{2222}][TFSI]$	161401-26-9	61.00 €/g	Sigma-Aldrich	[3]
$[C_{i3}mpyr][FSI]$	852620-97-4	25.00 €/g	Cymit Química	[3]
1-Cl-adamantane	935-56-8	10.56 €/g	Sigma-Aldrich	[4]
2-methyl-2-nitro-1-propanol	76-39-1	5.84 €/g	Cymit Química	[5]
$(CH_3)_2C(CH_2OH)_2$	126-30-7	1.59 €/g	Sigma-Aldrich	[6]
$NH_2C(CH_2OH)_3$	77-86-1	0.68 €/g	Fluorochem	[7]
$[CH_3NH_3][BF_4]$*	-	0.44 €/g	Sigma-Aldrich	This work
[DBA][BF4]*	-	0.35 €/g	Sigma-Aldrich	[8]

* Prices were estimated solely based on the quantities of reagents used to obtain 1 g of material. The purities of the reagents considered in each case are those listed in this work and in reference 8, respectively. DBA: $(CH_3(CH_2)_3)_2NH_2^+$

Table S2. Crystallographic data for $[CH_3NH_3][BF_4]$ at T = 100 K and 298 K.

	$[CH_3NH_3][BF_4]$ LT-phase	**$[CH_3NH_3][BF_4]$ RT-phase**
CCDC number	2454145	2454146
Empirical formula	CH_6NBF_4	CH_6NBF_4
Formula weight	118.88 g/mol	118.88 g/mol
Temperature	100.00 K	298.00 K
Crystal system	Monoclinic	Tetragonal
Space group	$P2_1/n$	P4/nmm
a	10.462(3) Å	5.33470(10) Å
b	7.3498(18) Å	5.33470(10) Å
c	12.266(3) Å	9.2028(4) Å
α	90°	90°
β	100.481(7)°	90°
γ	90°	90°
Volume	927.5(4) $Å^3$	261.903(15) $Å^3$
Z	8	2
ρ_{calc}	1.703 g/cm^3	1.431 g/cm^3
μ	0.213 mm^{-1}	0.186 mm^{-1}
F(000)	480.0	108.0
Crystal size	0.088 × 0.076 × 0.029 mm^3	0.088 × 0.076 × 0.029 mm^3
Radiation	MoKα (λ = 0.71073)	MoKα (λ = 0.71073)
2Θ range for data collection/°	4.714 to 50.794°	13.304 to 56.57°
Index ranges	-12 ≤ h ≤ 12 -8 ≤ k ≤ 8 -14 ≤ l ≤ 14	-7 ≤ h ≤ 6 -7 ≤ k ≤ 7 -12 ≤ l ≤ 12
Reflections collected	1632	5556
Independent reflections	1632 [R_{int} = 0.0, R_{sigma} = 0.1251]	202 [R_{int} = 0.0481, R_{sigma} = 0.0160]
Data / restraints /parameters	1632 / 0 / 119	202 / 0 / 27
Goodness-of-fit on F^2	1.113	2.045
Final R indexes [I>=2σ (I)]	R_1 = 0.1379 wR_2 = 0.2825	R_1 = 0.1265 wR_2 = 0.4133
Final R indexes [all data]	R_1 = 0.2098 wR_2 = 0.3130	R_1 = 0.1457 wR_2 = 0.4476
Largest diff. peak/hole	0.54 / -0.49 e $Å^{-3}$	0.12 / -0.18 e $Å^{-3}$

Table S3. Bond lengths for LT-phase (100 K) and RT-phase (298 K) of $[CH_3NH_3][BF_4]$.

F – B bonds		
Atom	**Atom**	**Length (Å)**
F001	B00D	1.392(14)
F002	B00D	1.389(14)
F006	B00D	1.384(13)
F008	B00D	1.400(14)
F003	B00E	1.409(14)
F004	B00E	1.385(13)
F005	B00E	1.404(14)
F007	B00E	1.385(14)
N – C bonds		
Atom	**Atom**	**Length (Å)**
N009	C00B	1.442(12)
N00A	C00C	1.459(13)

Table S4. Bond angles for LT-phase of $[CH_3NH_3][BF_4]$.

F – B bonds			
Atom	**Atom**	**Atom**	**Angle (°)**
F001	B00D	F008	110.1(10)
F002	B00D	F001	109.5(9)
F002	B00D	F008	108.3(9)
F006	B00D	F001	108.9(9)
F006	B00D	F002	110.3(10)
F006	B00D	F008	109.7(9)
F004	B00E	F003	108.7(10)
F004	B00E	F005	108.4(9)
F004	B00E	F007	111.2(9)
F005	B00E	F003	108.7(8)
F007	B00E	F003	109.2(9)
F007	B00E	F005	110.5(10)

Table S5. Transition temperature (T_t) and enthalpy (ΔH) of some representative materials belonging to the SS and SL-PCMs families presented in Figure 3a.

Material	Type	T_m[a)] (K)	ΔH (J g^{-1})	Reference
		SS-PCMs		
PE	Polyalcohol	458.4	339.5	[9]
NPG	Polyalcohol	315.4	119.1	[9]
TAM	Polyalcohol	405.4	295.6	[9]
C_{10}Mn	Layered hybrid perovskite	305.8	70.34	[9]
C_{12}Co	Layered hybrid perovskite	333.7-361	92.89	[9]
C_{14}Cu	Layered hybrid perovskite	342.2-352.5	163.99	[9]
C_{10}Zn	Layered hybrid perovskite	353.1-435.8-	100.92	[9]
SAN-g-PA	Polymeric	284.6-296.7	11.6-23.7	[9]
Cellulose-g-PEG	Polymeric	315.8-333.1	77.6-203.2	[9]
PUPCM	Polymeric	338.28	138.7	[9]
PEG/MDI/PVA	Polymeric	334.1	72.8	[9]
[C_{i3}mpyr][FSI]	Organic ionic plastic crystal	245	47	[3]
[N_{2222}][TFSI]	Organic ionic plastic crystal	277	45	[3]
[C_2mmor][FSI]	Organic ionic plastic crystal	283	68	[3]
[CH_3NH_3][BF_4]	Hybrid organic-inorganic plastic crystal	254	42	This work
1-Cl-adamantane	Organic plastic crystal	254	32	[4]
[DBA][BF_4][b)]	Hybrid organic-inorganic plastic crystal	269	58	[8]

Table S5. (continued)

Material	Type	T_m [a)] (K)	ΔH (J g^{-1})	Reference
		SL-PCMS		
$K_2PO_4 \cdot 6H_2O$	Salt hydrate	277	109	[10]
$LiClO_3 \cdot 3H_2O$	Salt hydrate	281.1	253	[10]
$KF \cdot 4H_2O$	Salt hydrate	291.5	231	[10]
Dodecane	Paraffin	263.4	216	[10]
Caprylic acid	Fatty acid	289	148.5	[10]
Paraffin C_{16}	Paraffin	289.7	237.1	[10]
Isopropyl stearate	Fatty acid derivate	287-291	140-142	[10]
Acetic acid	Fatty acid	289.7	184	[10]
51 wt% $ZnCl_2$	Inorganic eutectic mixture	210	116.84	[11]
17.1 wt% $MgCl_2$	Inorganic eutectic mixture	239.4	221.8	[11]
41.2 wt% NH_4NO_3	Inorganic eutectic mixture	255.6	186.29	[11]
10 wt% NaCl	Inorganic eutectic mixture	268.15	289	[11]
Tetradecane + octadecane	Organic eutectic mixture	268.98	227.52	[10]
Tetradecane + docosane	Organic eutectic mixture	274.5-278.6	234.33	[10]
Pentadecane + octadecane	Organic eutectic mixture	281.5-282	271.93	[10]
Pentadecane + docosane	Organic eutectic mixture	280.6-281.99	214.83	[10]

[a)]In this context, $T_t = T_m$ or melting temperature, as reported in the literature for most PCMs. [b)] Only the most energetic phase transition was considered.

Table S6. Barocaloric parameters of the different barocaloric materials represented in Figure 3b.

Material	T_t (K)	p (bar)	dT/dp (K kbar^{-1})	ΔS_{rev} (J K^{-1} kg^{-1})	ΔT_{rev} (K)	Reference
Metallic Alloys						
$LaFe_{11.33}Co_{0.47}Si_{1.2}$	250	2000	9.4	8.7 [a)]	-	12
$Gd_2Si_5Ge_5$	260	2000	3.5	6.2 [a)]	-	13
Mn_3NiN	262	2800	1.4	35 [a)]	3.4 [c)]	14
$Ni_{44.5}Co_{5.5}Mn_{35.5}In_{14.4}$	272	6000	4.4	15.6 [a)]	6 [c)]	15
$Ni_{0.95}Fe_{0.05}S$	274	1000	7.5	39.6 [a)]	8 [c)]	16
$Ni_{2.00}Mn_{1.32}In_{0.68}$	275	2500	1.88	4	3 [c)]	17
$Co_{50}Fe_{2.5}V_{31.5}Ga_{16}$	277	5000	2.5	31	6	18
$MnNiSi_{0.60}FeCoGe_{0.40}$	280	2300	7.3	47	4	19
$MnCoGeB_{0.03}$	286	2600	10	30	15 [c)]	20
Mn_3GaN	290	930	6.5	21.6 [a)]	1.3 [c)]	21
$Ni_{35.5}Co_{14.5}Mn_{35}Ti_{15}$	291	1000	5	8.5	4.2 [c)]	22
$Ni_{49.26}Mn_{36.08}In_{14.66}$	293	2500	1.8	10 [a)]	9.4 [c)]	23
$Ni_{0.875}Fe_{0.125}S$	294	1000	7.5	49.5 [a)]	-	16
Spin-Crossover Materials (SCO)						
$[FeL_2][BF4]_2$	257	430	15	68 [a)]	4	24
$[Fe(hyptrz)_3]A_2{\cdot}H_2O$	273	900	33.2	56 [a)]	10	25
Ammonium Salts						
NH_4I	268	800	81	71	34 [c)]	26
Organic Plastic Crystals						
$C_{10}H_{15}Cl$	254	1000	27.4	153	16.1	4
C_{60}	257	1000	17	32	9.7	1
o-carborane	277	600	30	79	14 [b)]	2
$[N_{2222}][TFSI]$	277	1000	23.7	160	-	3
$[C_2mmor][FSI]$	283	1000	12.1	184	-	3

Table S6. (continued)

Material	T_t (K)	p (bar)	dT/dp (K kbar^{-1})	ΔS_{rev} (J K^{-1} kg^{-1})	ΔT_{rev} (K)	Reference
Organic Plastic Crystals						
m-carborane	286	600	34	71	-	[2]
Hybrid Organic Inorganic Materials						
$[CH_3NH_3][BF_4]$	254	1000	24.9	175	13	This work
[DBA][BF_4]	269	1000	22.6	238	17	[8]
$(C_9H_{19}NH_3)_2MnCl_4$	294	1000	17.2	212	10	[27]

[a)]Isobaric entropy change; [b)]Adiabatic temperature change was calculated by indirect methods ($\Delta T_{rev} = \Delta S \cdot T_t / C_p$); [c)] Irreversible adiabatic temperature change.

References

1 J. Li, D. Dunstan, X. Lou, A. Planes, L. Mañosa, M. Barrio, J. L. Tamarit and P. Lloveras, Reversible barocaloric effects over a large temperature span in fullerite C_{60}, *J. Mater. Chem. A*, 2020, **8**, 20354–20362.

2 K. Zhang, R. Song, J. Qi, Z. Zhang, Z. Zhang, C. Yu, K. Li, Z. Zhang and B. Li, *Adv. Funct. Mater.*, , Colossal Barocaloric Effect in Carboranes as a Performance Tradeoff, *Adv. Funct. Mater.*, 2022, **32**, 2112622.

3 S. L. Piper, L. Melag, M. Kar, A. Sourjah, X. Xiao, E. F. May, K. F. Aguey-Zinsou, D. R. MacFarlane and J. M. Pringle, Organic ionic plastic crystals having colossal barocaloric effects for sustainable refrigeration, *Science*, 2025, **387**, 56–62.

4 A. Aznar, P. Negrier, A. Planes, L. Mañosa, E. Stern-Taulats, X. Moya, M. Barrio, J. L. Tamarit and P. Lloveras, Reversible colossal barocaloric effects near room temperature in 1-X-adamantane (X=Cl, Br) plastic crystals, *Appl. Mater. Today*, 2021, **23**, 101023.

5 A. Salvatori, M. Barrio, P. Negrier, S. Massip, M. Romanini, A. Aznar, P. Lloveras and J. L. Tamarit, Barocaloric response of plastic crystal 2-methyl-2-nitro-1-propanol across and far from the solid-solid phase transition, *J. Phys. Energy,* 2023, **5**, 045015.

6 P. Lloveras, A. Aznar, M. Barrio, P. Negrier, C. Popescu, A. Planes, L. Mañosa, E. Stern-Taulats, A. Avramenko, N. D. Mathur, X. Moya and J. L. Tamarit, , Colossal barocaloric effects near room temperature in plastic crystals of neopenthylglycol, *Nat. Commun.*, 2019, **10**, 1803

7 A. Aznar, P. Lloveras, M. Barrio, P. Negrier, A. Planes, L. Mañosa, N. D. Mathur, X. Moya and J. L. Tamarit, Reversible and irreversible colossal barocaloric effects in plastic crystals, *J. Mater. Chem. A*, 2020, **8**, 639–647..

8 J. García-Ben, J. M. Bermúdez-García, R. J. C. Dixey, I. Delgado-Ferreiro, A. L. Llamas-Saiz, J. López-Beceiro, R. Artiaga, A. García-Fernández, U. B. Cappel, B. Alonso, S. Castro-García, A. E. Phillips, M. Sánchez-Andújar and M. A. Señarís-Rodríguez, Structure and thermal property relationships in the thermomaterial di-n-butylammonium tetrafluoroborate for multipurpose cooling and cold-storage, *J. Mater. Chem. A*, 2023, **11**, 22232–22247.

9 A. Fallahi, G. Guldentops, M. Tao, S. Granados-Focil and S. Van Dessel, Review on solid-solid phase change materials for thermal energy storage: Molecular structure and thermal properties, *Appl. Therm. Eng.*, 2017, **127**, 1427–1441.

10 E. Oró, A. de Gracia, A. Castell, M. M. Farid and L. F. Cabeza, Review on phase change materials (PCMs) for cold thermal energy storage applications, *Appl. Energy*, 2012, **99**, 513–533.

11 L. Yang, U. Villalobos, B. Akhmetov, A. Gil, J. O. Khor, A. Palacios, Y. Li, Y. Ding, L. F. Cabeza, W. L. Tan and A. Romagnoli, A comprehensive review on sub-zero temperature cold thermal energy storage materials, technologies, and applications: State of the art and recent developments**,** *Appl. Energy*, 2021, **288**, 116555.

12 L. Mañosa, D. González-Alonso, A. Planes, M. Barrio, J. L. Tamarit, I. S. Titov, M. Acet, A. Bhattacharyya and S. Majumdar, Inverse barocaloric effect in the giant magnetocaloric La-Fe-Si-Co compound, *Nat. Commun.*, 2011, **2**, 595.

13 S. Yuce, M. Barrio, B. Emre, E. Stern-Taulats, A. Planes, J. L. Tamarit, Y. Mudryk, K. A. Gschneidner, V. K. Pecharsky and L. Mañosa, Barocaloric effect in the magnetocaloric prototype $Gd_5Si_2Ge_2$, *Appl. Phys. Lett.*, 2012, **101**, 071906.

14 D. Boldrin, E. Mendive-Tapia, J. Zemen, J. B. Staunton, T. Hansen, A. Aznar, J. L. Tamarit, M. Barrio, P. Lloveras, J. Kim, X. Moya and L. F. Cohen, Multisite Exchange-Enhanced Barocaloric Response in Mn_3NiN, *Phys. Rev. X*, 2018, **8**, 041035.

15 X. He, S. Wei, Y. Kang, Y. Zhang, Y. Cao, K. Xu, Z. Li and C. Jing, Enhanced barocaloric effect produced by hydrostatic pressure-induced martensitic transformation for $Ni_{44.6}Co_{5.5}Mn_{35.5}In_{14.4}$ Heusler alloy, *Scr. Mater.*, 2018, **145**, 58–61.

16 J. Lin, P. Tong, X. Zhang, Z. Wang, Z. Zhang, B. Li, G. Zhong, J. Chen, Y. Wu, H. Lu, L. He, B. Bai, L. Ling, W. Song, Z. Zhang and Y. Sun, Giant room-temperature barocaloric effect at the electronic phase transition in $Ni_{1-x}Fe_xS$, *Mater. Horiz.*, 2020, **7**, 2690–2695.

17 E. Stern-Taulats, A. Planes, P. Lloveras, M. Barrio, J. L. Tamarit, S. Pramanick, S. Majumdar, S. Yüce, B. Emre, C. Frontera and L. Mañosa, Tailoring barocaloric and magnetocaloric properties in low-hysteresis magnetic shape memory alloys, *Acta Mater.*, 2015, **96**, 324–332.

18 H. Liu, Z. Li, Y. Zhang, Z. Ni, K. Xu and Y. Liu, A large barocaloric effect associated with paramagnetic martensitic transformation in $Co_{50}Fe_{2.5}V_{31.5}Ga_{16}$, *Scr. Mater.*, 2020, **177**, 1–5.

19 P. Lloveras, T. Samanta, M. Barrio, I. Dubenko, N. Ali, J. L. Tamarit and S. Stadler, Giant reversible barocaloric response of $(MnNiSi)_{1-x}(FeCoGe)_x$ (x = 0.39, 0.40, 0.41), *APL Mater.*, 2019, **7**, 061106.

20 A. Aznar, P. Lloveras, J. Y. Kim, E. Stern-Taulats, M. Barrio, J. L. Tamarit, C. F. Sánchez-Valdés, J. L. Sánchez Llamazares, N. D. Mathur and X. Moya, Giant and Reversible Inverse Barocaloric Effects near Room Temperature in Ferromagnetic $MnCoGeB_{0.03}$, *Adv. Mater.*, 2019, **31**, 1903577.

21 D. Matsunami, A. Fujita, K. Takenaka and M. Kano, Giant barocaloric effect enhanced by the frustration of the antiferromagnetic phase in Mn_3GaN, *Nat. Mater.*, 2015, 14, 73–78.

22 Z. Wei, Y. Shen, Z. Zhang, J. Guo, B. Li, E. Liu, Z. Zhang and J. Liu, , Low-pressure-induced giant barocaloric effect in an all-d-metal Heusler $Ni_{35.5}Co_{14.5}Mn_{35}Ti_{15}$, *APL Mater.*, 2020, 8, 051101.

23 L. Mañosa, D. González-Alonso, A. Planes, E. Bonnot, M. Barrio, J. L. Tamarit, S. Aksoy and M. Acet, Giant solid-state barocaloric effect in the Ni-Mn-In magnetic shape-memory alloy, *Nat. Mater.*, 2010, **9**, 478–481.

24 S. P. Vallone, A. N. Tantillo, A. M. dos Santos, J. J. Molaison, R. Kulmaczewski, A. Chapoy, P. Ahmadi, M. A. Halcrow and K. G. Sandeman, Giant Barocaloric Effect at the Spin Crossover Transition of a Molecular Crystal, *Adv. Mater.*, 2019, **31**, 1807334.

25 P. J. Von Ranke, B. P. Alho, R. M. Ribas, E. P. Nobrega, A. Caldas, V. S. R. De Sousa, M. V. Colaço, L. F. Marques, D. L. Rocco and P. O. Ribeiro, Colossal refrigerant capacity in $[Fe(hyptrz)_3]A_2 \cdot H_2O$ around the freezing temperature of water, *Phys. Rev. B*, 2018, **98**, 224408.

26 Q. Ren, J. Qi, D. Yu, Z. Zhang, R. Song, W. Song, B. Yuan, T. Wang, W. Ren, Z. Zhang, X. Tong and B. Li, Ultrasensitive barocaloric material for room-temperature solid-state refrigeration*, Nat. Commun.*, 2022, **13**, 2293

27 Y. Gao, H. Liu, F. Hu, H. Song, H. Zhang, J. Hao, X. Liu, Z. Yu, F. Shen, Y. Wang, H. Zhou, B. Wang, Z. Tian, Y. Lin, C. Zhang, Z. Yin, J. Wang, Y. Chen, Y. Li, Y. Song, Y. Shi, T. Zhao, J. Sun, Q. Huang and B. ShenReversible colossal barocaloric effect dominated by disordering of organic chains in in $(CH_3–(CH_2)_{n-1}–NH_3)_2MnCl_4$ single crystals, *NPG Asia Mater.*, 2022, **14**, 34.